

Grading diffuse gliomas without intense contrast enhancement by amide proton transfer MR imaging: comparisons with diffusion- and perfusion-weighted imaging

Osamu Togao¹ · Akio Hiwatashi¹ · Koji Yamashita¹ · Kazufumi Kikuchi¹ · Jochen Keupp² · Koji Yoshimoto³ · Daisuke Kuga³ · Masami Yoneyama⁴ · Satoshi O. Suzuki⁵ · Toru Iwaki⁵ · Masaya Takahashi⁶ · Koji Iihara³ · Hiroshi Honda¹

Received: 9 December 2015 / Revised: 19 February 2016 / Accepted: 9 March 2016 / Published online: 22 March 2016
© European Society of Radiology 2016

Abstract

Objectives To investigate whether amide proton transfer (APT) MR imaging can differentiate high-grade gliomas (HGGs) from low-grade gliomas (LGGs) among gliomas without intense contrast enhancement (CE).

Methods This retrospective study evaluated 34 patients (22 males, 12 females; age 36.0 ± 11.3 years) including 20 with LGGs and 14 with HGGs, all scanned on a 3T MR scanner. Only tumours without intense CE were included. Two neuro-radiologists independently performed histogram analyses to measure the 90th-percentile (APT₉₀) and mean (APT_{mean}) of the tumours' APT signals. The apparent diffusion coefficient (ADC) and relative cerebral blood volume (rCBV) were also measured. The parameters were compared between the groups

with Student's t-test. Diagnostic performance was evaluated with receiver operating characteristic (ROC) analysis.

Results The APT₉₀ (2.80 ± 0.59 % in LGGs, 3.72 ± 0.89 % in HGGs, $P=0.001$) and APT_{mean} (1.87 ± 0.49 % in LGGs, 2.70 ± 0.58 % in HGGs, $P=0.0001$) were significantly larger in the HGGs compared to the LGGs. The ADC and rCBV values were not significantly different between the groups. Both the APT₉₀ and APT_{mean} showed medium diagnostic performance in this discrimination.

Conclusions APT imaging is useful in discriminating HGGs from LGGs among diffuse gliomas without intense CE.

Key Points

- Amide proton transfer (APT) imaging helps in grading non-enhancing gliomas
- High-grade gliomas showed higher APT signal than low-grade gliomas
- APT imaging showed better diagnostic performance than diffusion- and perfusion-weighted imaging

✉ Akio Hiwatashi
hiwatashi@radiol.med.kyushu-u.ac.jp

¹ Department of Clinical Radiology, Graduate School of Medical Sciences, Kyushu University, 3-1-1 Maidashi Higashi-ku, Fukuoka 812-8582, Japan

² Philips Research, Röntgenstrasse 24-26, Hamburg 22335, Germany

³ Department of Neurosurgery, Graduate School of Medical Sciences, Kyushu University, 3-1-1 Maidashi Higashi-ku, Fukuoka 812-8582, Japan

⁴ Philips Electronics Japan, 2-13-37 Konan Minato-ku, Tokyo 108-8507, Japan

⁵ Department of Neuropathology, Graduate School of Medical Sciences, Kyushu University, 3-1-1 Maidashi Higashi-ku, Fukuoka 812-8582, Japan

⁶ Advanced Imaging Research Center, UT Southwestern Medical Center, 2201 Inwood Rd, Dallas, TX 75235, USA

Keywords Amide proton transfer imaging · Chemical exchange saturation transfer · MR imaging · Brain tumour · Glioma

Abbreviations

APT	Amide proton transfer
LGG	Low-grade gliomas
HGG	High-grade glioma
CE	Contrast enhancement
ADC	Apparent diffusion coefficient
rCBV	relative cerebral blood volume
ROC	Receiver operating characteristic
DSC	Dynamic susceptibility contrast
PW	Perfusion-weighted

DW	Diffusion-weighted
CEST	Chemical exchange saturation transfer
WHO	World Health Organization
GBM	Glioblastoma multiforme
RF	Radiofrequency
TR	Repetition time
TE	Echo time
FOV	Field of view
2D	Two dimensional
NAWM	Normal-appearing white matter
FLAIR	Fluid attenuation inversion recovery
MTR _{asym}	Asymmetry of the magnetization transfer ratio
ROI	Region-of-interest
ICC	Intra-class correlation coefficient
AUC	Area under the curve
3D	Three-dimensional

Introduction

Gliomas are the most frequent primary brain neoplasms, varying histopathologically from low to high grades [1]. The differentiation between low-grade glioma (LGG, grade II) and high-grade glioma (HGG, grades III, IV) is clinically important, since the prognosis and the therapeutic strategy could substantially differ depending on the grade. Because of their dismal prognosis, HGGs are usually treated with surgical resection followed by adjuvant radiation therapy and chemotherapy [2]. HGGs misdiagnosed as LGGs will be treated less aggressively than necessary, and vice versa.

The preoperative imaging of diffuse gliomas with estimation of the grade is also important since there can be inherent sampling errors associated with intratumoral histological heterogeneity in gliomas. Inappropriate sampling from sites with a lower histological grade in a tumour may lead to the underestimation of the true grades. Such sampling errors could occur especially in patients who undergo biopsy. Moreover, a 2014 study revealed that a MR imaging biomarker such as the relative cerebral blood volume (rCBV) measured by dynamic susceptibility contrast (DSC) perfusion-weighted (PW) imaging better predicted the prognosis of patients with diffuse gliomas than histology [3], indicating the possibility of superior performance of imaging over histopathology in predicting glioma outcomes.

Traditionally, the presence and degree of contrast enhancement (CE) after the administration of a gadolinium-based contrast agent on MR imaging have been used as characteristics of the malignancy of diffuse gliomas [4, 5]. Typically, HGGs show moderate-to-strong CE, whereas LGGs exhibit no or mild CE. However, the degree of CE of gliomas is not always reliable for the differentiation between LGGs and HGGs, presumably because the CE of gliomas may result from a disruption of the blood-brain barrier rather than neovascularization.

The grading of nonenhancing gliomas by conventional MR imaging methods has been challenging. It was reported that approximately 20 % of LGGs enhanced after the administration of a gadolinium-based contrast agent, whereas 14 %–45 % of nonenhancing gliomas were histologically proved to be HGGs [6, 7]. It was reported that diffusion-weighted (DW) or PW imaging could differentiate HGGs from LGGs in nonenhancing gliomas [8, 9], but no consensus has been reached in light of the limited number of studies.

Amide proton transfer (APT) imaging was developed as one of the endogenous chemical exchange saturation transfer (CEST) imaging techniques [10, 11]. Since grades of diffuse gliomas are associated with the presence of mitosis and degree of cell density, the unique amide proton-based contrast mechanism may be able to detect the increase in concentrations of proteins and peptides in higher grades of diffuse gliomas. This method may be useful in grading gliomas in a different way from previous MR methods. The APT method allows noninvasive imaging of the proton exchange between bulk-water and the amide protons (-NH) of endogenous mobile proteins and peptides [10, 11]. It was demonstrated that APT imaging is useful for grading gliomas [12–14], but no detailed analysis including other imaging findings has been performed, to our knowledge. The purpose of the present study was to determine whether APT imaging could differentiate HGGs from LGGs among gliomas without intense CE. We compared the diagnostic performance of APT imaging in this discrimination with that of DW imaging and DSC PW imaging.

Materials and methods

Patients

This retrospective study was approved by the institutional review board of Kyushu University Hospital, and the requirement for informed consent was waived. APT imaging has been a part of our routine preoperative MR imaging protocol for brain tumours since August 2011. The preoperative MR imaging data of the 91 consecutive patients with diffuse gliomas who were identified between September 2011 and July 2015 were analyzed. The histopathologic diagnosis and grades were determined with resected or biopsy specimens according to the WHO criteria by two established neuropathologists (S.O.S. and T.I. with 22 and 31 years of experience, respectively), who were blinded to the imaging findings. A total of 34 patients including 20 with LGGs (World Health Organization [WHO] grade II, 13 males and seven females; mean age 36.0 ± 11.5 years) and 14 with HGGs (WHO grade III or IV, nine males and five females; mean age 39.0 ± 13.3 years) were identified. The characteristics of patients are described in Table 1.

Table 1 Patient Characteristics

	Patients	Age (year-old)	Sex	WHO Grade	Histology	Location	Maximum Diameter (mm)	Biopsy or Resection	Contrast Enhancement	
									Observer1	Observer2
LGG	1	56	M	II	O	rt. frontal	59	Total Resection	None	None
	2	59	F	II	O	rt. frontal	28	Total Resection	None	None
	3	23	M	II	O	bil. frontal	54	Resection (75 %)	Slight	Slight
	4	42	F	II	A	rt. temporal	35	Total Resection	Slight	None
	5	38	M	II	A	lt. frontal	36	Total Resection	None	None
	6	33	M	II	A	rt. parietal	38	Total Resection	None	None
	7	32	M	II	OA	rt. frontal	61	Total Resection	None	None
	8	33	M	II	A	lt. frontal	46	Total Resection	None	None
	9	39	F	II	A	lt. temporal	59	Total Resection	None	Slight
	10	12	M	II	A	bil. thalamus	32	Needle Biopsy	Slight	Slight
	11	33	F	II	A	lt. occipital	24	Total Resection	None	None
	12	30	M	II	A	lt. frontal	31	Resection (95 %)	None	None
	13	23	M	II	A	lt. frontal	48	Total Resection	None	None
	14	29	M	II	O	rt. temporal	31	Total Resection	None	None
	15	38	M	II	A	rt. frontal	40	Resection (90 %)	None	None
	16	37	M	II	O	rt. frontal	52	Total Resection	None	None
	17	45	F	II	O	rt. frontal	74	Resection (80 %)	None	None
	18	45	F	II	A	rt. temporal	41	Resection (90 %)	None	None
	19	49	F	II	O	rt. frontal	61	Total Resection	None	None
	20	24	M	II	A	lt. frontal	26	Total Resection	None	None
HGG	1	45	F	III	AO	rt. frontal	36	Total Resection	None	None
	2	25	F	III	AO	rt. frontal	43	Total Resection	Slight	Slight
	3	39	M	III	AOA	rt. frontal	55	Total Resection	None	None
	4	39	M	III	AA	brain stem, lt. cerebellum	73	Open Biopsy	None	None
	5	28	M	III	AA	brain stem, bil. cerebellum	37	Open Biopsy	None	None
	6	38	F	IV	GBM	lt. insula	63	Resection (75 %)	None	None
	7	37	F	III	AOA	lt. frontal	61	Resection (75 %)	None	None
	8	14	M	IV	GBM	lt. thalamus	45	Resection (80 %)	Slight	Slight
	9	38	M	IV	GBM	rt. temporal	80	Resection (80 %)	Slight	Slight
	10	38	M	III	AA	lt. insula	64	Resection (90 %)	None	None
	11	47	M	III	AO	lt. insula	36	Resection (90 %)	Slight	None
	12	74	M	III	Gliomatosis	lt. cerebrum	101	Open Biopsy	None	None
	13	40	M	IV	GBM	rt. insula, basal ganglia	66	Resection (50 %)	Slight	Slight
	14	44	F	III	AA	rt frontal	30	Total Resection	None	None

Abbreviations: LGG, low-grade glioma; HGG, high-grade glioma; M, male; F, female; O, oligodendroglioma; A, diffuse astrocytoma; OA, oligoastrocytoma; AO, anaplastic oligodendroglioma; AA, anaplastic astrocytoma; AOA, anaplastic oligoastrocytoma; GBM, glioblastoma multiforme; rt., right; lt., left

The patients' histological types of gliomas were as follows: 12 diffuse astrocytomas, seven oligodendrogliomas, one oligoastrocytoma, four anaplastic astrocytomas, three anaplastic oligodendrogliomas, two anaplastic oligoastrocytomas, one gliomatosis cerebri, and four glioblastoma multiforme (GBMs). All patients underwent contrast-enhanced T1-weighted imaging, APT, DW, and DSC PW imaging in their preoperative examinations. The interval between the MR imaging and the surgery was <2 weeks in all patients.

MR imaging

MR imaging was performed on a 3T clinical scanner (Achieva TX, Philips Healthcare, Best, The Netherlands) equipped with a pencil-beam, second-order shim, using an eight-channel head coil for signal reception and two-channel parallel transmission via the body coil for radiofrequency (RF) transmission. For the APT imaging, the acquisition software was modified to alternate the operation of the two transmission

channels during the RF saturation pulse, which enables long quasi-continuous RF saturation at a 100 % RF duty-cycle and a special RF shimming for the saturation homogeneity of the alternated pulse [15, 16].

On a single axial slice corresponding to a maximum cross-section area of a tumour, two-dimensional (2-D) APT imaging was performed using a saturation pulse with a duration of 2 s (40×50 msec, sinc-gauss-shaped elements) and a saturation power level of $B_{1,rms} = 2.0 \mu\text{T}$ [15, 16]. For acquiring a Z-spectrum, the imaging was repeated at 25 saturation frequency offsets from $\omega = -6$ to $+6$ ppm with a step of 0.5 ppm as well as one far-off-resonant frequency ($\omega = -1560$ ppm) for signal normalization.

The other imaging parameters were as follows: Fast spin-echo (FSE) readout with driven equilibrium refocusing; echo train length (ETL)=128; sensitivity encoding factor=2; repetition time (TR)=5,000 msec; echo time (TE)=6 msec; matrix=128 × 128 (reconstructed to 256 × 256); slice thickness=5 mm, field of view (FOV)=230 × 230 mm; scan time=2 min 20 s for one Z-spectrum. A ΔB_0 map for off-resonance correction was acquired separately using a 2D gradient-echo with identical spatial resolution for a point-by-point ΔB_0 correction [15, 16].

The DW imaging was performed in the axial plane with a single-shot spin-echo echo planar imaging sequence with the following parameters: TR=4,136 msec; TE=70 msec; matrix=160 × 126 (reconstructed to 256 × 256); slice thickness=5 mm, FOV=230 × 230 mm; scan time=50 s, b-values; 0 and 1000 (sec/mm^2). The apparent diffusion coefficient (ADC) was calculated by mono-exponential fitting with the pair of b-values.

The DSC PW imaging was conducted after the administration of 0.05 mmol/kg gadolinium (Gd) contrast agent (gadopentetate dimeglumine; Bayer Health Care, Osaka, Japan or gadodiamide; Daiichi-Sankyo Pharmaceutical, Tokyo, Japan) as a preload dose to minimize T1 leakage effects [17]. During the acquisition, an additional 0.05 mmol/kg bolus was administered at 5 mL/s. The DSC PW imaging was obtained with a gradient-echo echo-planar imaging sequence in the axial plane using the following parameters: TR=1,428 msec; TE=35 msec; matrix=288 × 288; slice thickness=5 mm, FOV=230 × 230 mm; number of slices=22, sensitivity encoding factor 2; scan time=1 min 26 s.

Relative cerebral blood volume (rCBV) maps were generated using an Osirix workstation (v. 5.0.2, 64 bit; <http://www.osirix-viewer.com/>) with IB Neuro software (ver.1; Imaging Biometrics, Elm Grove, WI) to calculate the whole-brain CBV from the DSC PW imaging data [18]. Briefly, after excluding the first four time points of each DSC PW imaging data set due to saturation effects, signal intensities were normalized to

the baseline and then converted to the change in relaxivity over time [$\Delta R_2^*(t)$] for the entire brain. The CBV was calculated voxel-by-voxel by integrating the area under the $\Delta R_2^*(t)$ curve, ending at the time point 40 s after the nadir signal intensity of the first pass-bolus. All CBV values were corrected for T1-weighted leakage with preload dosing, and a modeling algorithm was used to correct T2/T2*-weighted residual effects [19]. The CBV maps were normalized to contralateral normal-appearing white matter (NAWM) to create rCBV maps.

For reference, standard MR images, including T1-weighted (TR=500 msec, TE=10 msec, matrix=256 × 271, 22 slices), T2-weighted (TR=3,000 msec, TE=80 msec, ETL=8, matrix=512 × 416, 22 slices), fluid attenuation inversion recovery (FLAIR, TR=10,000 msec, TE=120 msec, Inversion time=2,700 msec, ETL=27, matrix=320 × 211, 22 slices), and contrast enhanced T1-weighted images (TR=500 msec, TE=20 msec, matrix=256 × 271, 22 slices) were acquired in the axial plane. The FOV size (230 × 230 mm) and the slice thickness (5 mm) are identical in these images. The APT images were acquired before the administration of the gadolinium contrast agent.

Two experienced neuroradiologists (O.T. and K.Y., 15 and 13 years of experience in neuroradiology, respectively) independently reviewed and evaluated the degree of CE after the administration of a gadolinium-based contrast agent to each tumour. The degree of CE was visually graded on a six-point scale: 0, none; 1, slight; 2, mild; 3, moderate; 4, distinct; and 5; strong. Only patients with a glioma that showed no (grade 0) or slight (grade 1) CE judged by both observers were included in this study. The inter-rater agreement statistic (Kappa) for the evaluation of CE was 0.82.

APT imaging processing

The APT signal is defined as asymmetry of the magnetization transfer ratio at 3.5 ppm: $\text{MTR}_{\text{asym}}(3.5 \text{ ppm})$ [11].

$\text{APT signal} = \text{MTR}_{\text{asym}}(3.5 \text{ ppm})$

$$= [S_{\text{sat}}(-3.5 \text{ ppm}) - S_{\text{sat}}(+3.5 \text{ ppm})] / S_0, \quad (1)$$

where $S_{\text{sat}}(-3.5 \text{ ppm})$, $S_{\text{sat}}(+3.5 \text{ ppm})$, and S_0 are the signal intensities obtained at -3.5 , $+3.5$, and -1560 ppm, respectively [10]. All image data were analyzed with the software program ImageJ (version 1.43u; National Institutes of Health, Bethesda, MD). A plug-in was created to assess the Z-spectra and MTR_{asym} equipped with a correction function for B_0 inhomogeneity, using interpolation among the Z-spectral image data.

First, rigid body motion correction was performed using the TurboReg algorithm [20]. The local B0 field shift in Hz was obtained from the B0 map, which was created from dual-echo gradient echo images ($\Delta TE = 1$ msec), and each voxel was corrected in image intensity for the nominal saturation frequency offset by Lagrange interpolation among the neighboring Z-spectral images. This procedure corresponds to a frequency shift along the saturation frequency offset axis according to the measured B0 shift. Finally, the APT-weighted image was calculated by Eq. (1) described above.

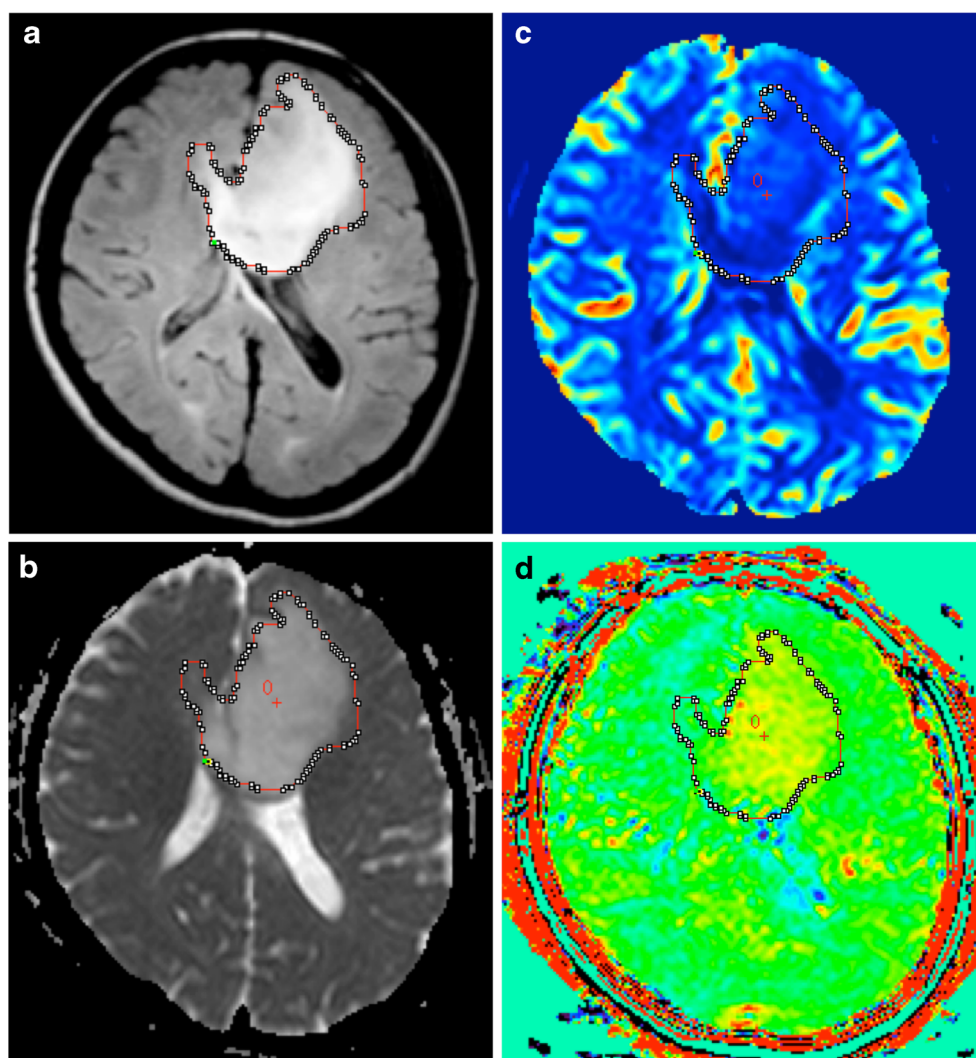
Image analysis

The APT-weighted image, ADC map, rCBV map, and FLAIR image of each patient were co-registered to the raw image of the APT image with the rigid body registration using the TurboReg algorithm [20]. This registration procedure performed fine adjustments for locations and angles on two types of single-slice image. In this process, the distance between any pair of points images was

conserved, and the voxel value did not change. On the FLAIR image, areas showing high signal intensity were manually segmented independently by the two neuroradiologists (O.T. and K.Y.) with the software program Medical Image Processing, Analysis and Visualization (MIPAV, version 7.0.1, Centre for Information Technology, U.S. National Institutes of Health, Bethesda, MD). The segmented regions were copied from the FLAIR image and pasted to the APT-weighted image, the ADC map, and the rCBV map (Fig. 1).

The areas with obvious artifacts or signals from a blood vessel were excluded from the segmented area. The APT signal, ADC, and rCBV were measured in all pixels included in the segmented region. The 90th percentile for APT (APT_{90}) and the 90th percentile for rCBV ($rCBV_{90}$), and the 10th percentile for ADC (ADC_{10}) were derived by the histogram approach in the segmented region. The $rCBV_{90}$ and ADC_{10} correspond to the maximum rCBV and minimum ADC in previous region-of-interest (ROI)-based studies, respectively. The mean values for the parameters (APT_{mean} , ADC_{mean} ,

Fig. 1 Segmentation of the tumours. After the co-registration of all images, areas showing a hyperintense signal on the FLAIR image (a) were manually segmented independently by the two observers. The segmented regions were copied from the FLAIR image and pasted to the ADC map (b), and the rCBV map (c), and the APT-weighted image (d)



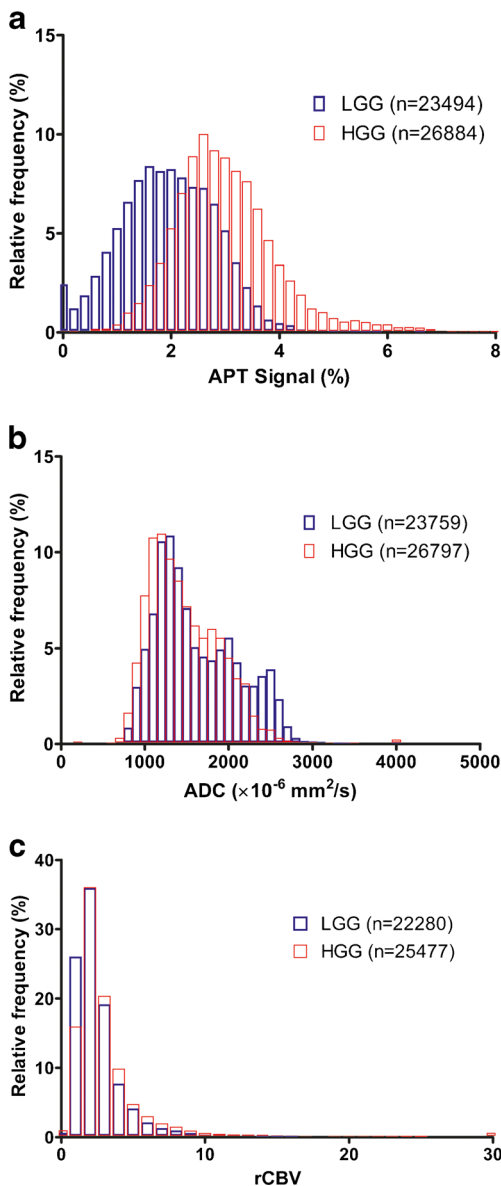


Fig. 2 Histogram profiles over all pixels in the patients. The normalized histogram analysis of the APT signal (a) over all pixels in tumour ROIs (LGG: 23,494 pixels, HGG: 26,884 pixels) revealed that the overall histogram profile shifted towards the higher APT signal in the HGG group in comparison with the LGG group, and a heavy-tailed distribution was observed in the HGG group. The normalized histogram analysis of the ADCs (b) and rCBV (c) values over all pixels in the tumour ROIs resulted in similar profiles for both groups, but there were pixels with a higher ADC or a lower rCBV in the LGG group

rCBV_{mean}) were also calculated. No necrosis, hemorrhage, or cysts were identified on the MR images in any patients.

Statistical analysis

All values are expressed as mean ± standard deviation (SD). The APT signals, ADC values, and rCBV values

Table 2 Inter-observer agreement

	ICC
APT ₉₀	0.989
ADC ₁₀	0.638
rCBV ₉₀	0.886
APT _{mean}	0.935
ADC _{mean}	0.971
rCBV _{mean}	0.921

Abbreviations: ICC, intraclass correlation coefficient; APT₉₀, 90-percentile value of APT signal; ADC₁₀, 10-percentile value of ADC; rCBV₉₀, 90-percentile value of rCBV; APT_{mean}, mean value of APT signal; ADC_{mean}, mean value of ADC; rCBV_{mean}, mean value of rCBV

were compared between the LGG and HGG groups using Student’s t-test. The size of segmented region was compared between the two observers using the paired t-test. The inter-observer agreement regarding the measurements by the two observers was analyzed by calculating the intra-class correlation coefficient (ICC). ICCs are considered to be excellent if >0.74 [21]. The measurements by the two observers for each patient were averaged for further analysis. The comparisons of measurements between the LGGs and HGGs were performed with Student’s t-test. Correlations among the APT signals, ADC values, and rCBV values were evaluated with Pearson’s correlation coefficient.

Receiver operating characteristic (ROC) curve analyses were conducted to evaluate the diagnostic performance of the parameters in differentiating LGGs from HGGs. We considered area under the curve (AUC) values <0.7, 0.7–0.9, and >0.9 to indicate low, medium, and high diagnostic performance, respectively. Statistical analyses were performed with a commercially available

Table 3 Measurements of APT signal, ADC, and rCBV in LGGs and HGGs

	LGG (n=20)	HGG (n=14)	P-value
APT ₉₀ (%)	2.80 ± 0.59	3.72 ± 0.89	0.001
ADC ₁₀ (×10 ⁻³ mm ² /s)	1.11 ± 0.15	1.11 ± 0.22	0.97
rCBV ₉₀	4.06 ± 1.47	5.01 ± 3.08	0.2718
APT _{mean} (%)	1.87 ± 0.49	2.70 ± 0.58	0.0001
ADC _{mean} (×10 ⁻³ mm ² /s)	1.58 ± 0.32	1.47 ± 0.31	0.33
rCBV _{mean}	2.01 ± 0.68	2.57 ± 1.33	0.16

Abbreviations: LGGs, low-grade gliomas; HGGs, high-grade gliomas; APT₉₀, 90-percentile value of APT signal; ADC₁₀, 10-percentile value of ADC; rCBV₉₀, 90-percentile value of rCBV; APT_{mean}, mean value of APT signal; ADC_{mean}, mean value of ADC; rCBV_{mean}, mean value of rCBV

Table 4 Receiver Operating Characteristic Curve Analysis for Differentiation of LGGs and HGGs

	AUC	Cutoff Value	Sensitivity (%)	Specificity (%)	Z-statistics	Significance Level (<i>p</i>)
APT ₉₀	0.811*	2.92 (%)	85.7	70.0	4.059*	<0.0001
ADC ₁₀	0.536	0.93 ($\times 10^{-3}$ mm ² /s)	28.6	95.9	0.316	0.75
rCBV ₉₀	0.545	6.20	35.7	100.0	0.396	0.69
APT _{mean}	0.886 ⁺	2.56 (%)	71.4	95.0	6.611*	<0.0001
ADC _{mean}	0.593	1.20 ($\times 10^{-3}$ mm ² /s)	35.7	85.0	0.902	0.37
rCBV _{mean}	0.568	2.94	35.7	94.7	0.606	0.55

*, *P* < .05 compared with ADC₁₀ and rCBV₉₀; ⁺, *P* < .05 compared with ADC_{mean} and rCBV_{mean}

Abbreviations: AUC, area under the curve; APT₉₀, 90-percentile value of APT signal; ADC₁₀, 10 percentile value of ADC; rCBV₉₀, 90-percentile value of rCBV; APT_{mean}, mean value of APT signal; ADC_{mean}, mean value of ADC; rCBV_{mean}, mean value of rCBV

software package (SPSS, IBM 19, Armonk, NY; Prism 5.0, GraphPad Software, San Diego, CA; and MedCalc

v. 13.1.2.0, Broekstraat, Mariakerke, Belgium). *P*-values < 0.05 were considered significant.

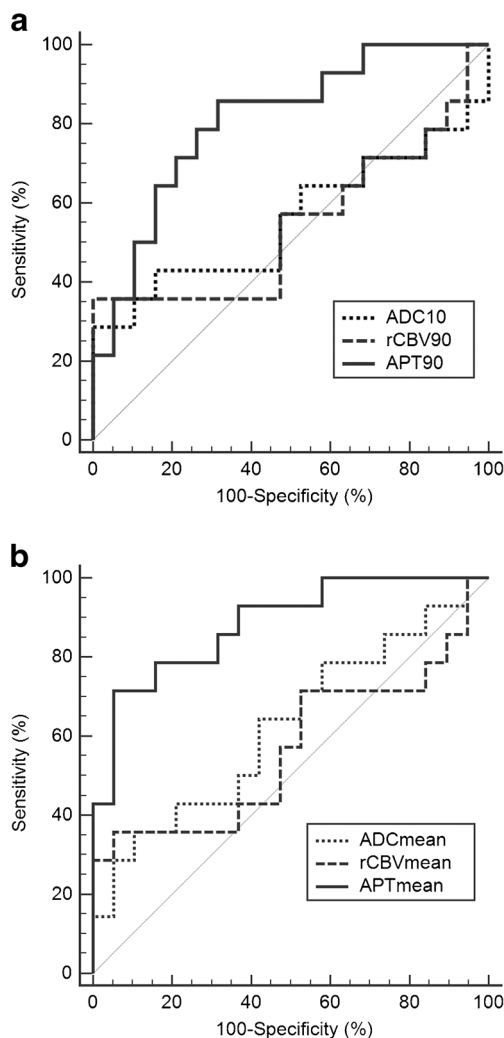


Fig. 3 Receiver operating characteristic curve analyses in differentiating LGGs from HGGs. (a) APT₉₀ showed medium diagnostic performance, whereas ADC₁₀ and rCBV₉₀ showed low diagnostic performance. (b) APT_{mean} showed medium diagnostic performance, whereas ADC_{mean} and rCBV_{mean} showed low diagnostic performance

Results

Histogram analysis

Figure 2 demonstrates the histogram profiles over all pixels in the patients as obtained by one of the two observers. Our normalized histogram analysis of the APT signal over all pixels in tumour ROIs (LGG: 23,494 pixels, HGG: 26,884 pixels) revealed that the overall histogram profile shifted towards the higher APT signal in the HGG group in comparison with the LGG group, and a heavy-tailed distribution was observed in the HGG group. The normalized histogram analysis of the ADCs and rCBV values over all pixels in the tumour ROIs resulted in similar profiles for both groups, but there were pixels with a higher ADC or a lower rCBV in the LGG group.

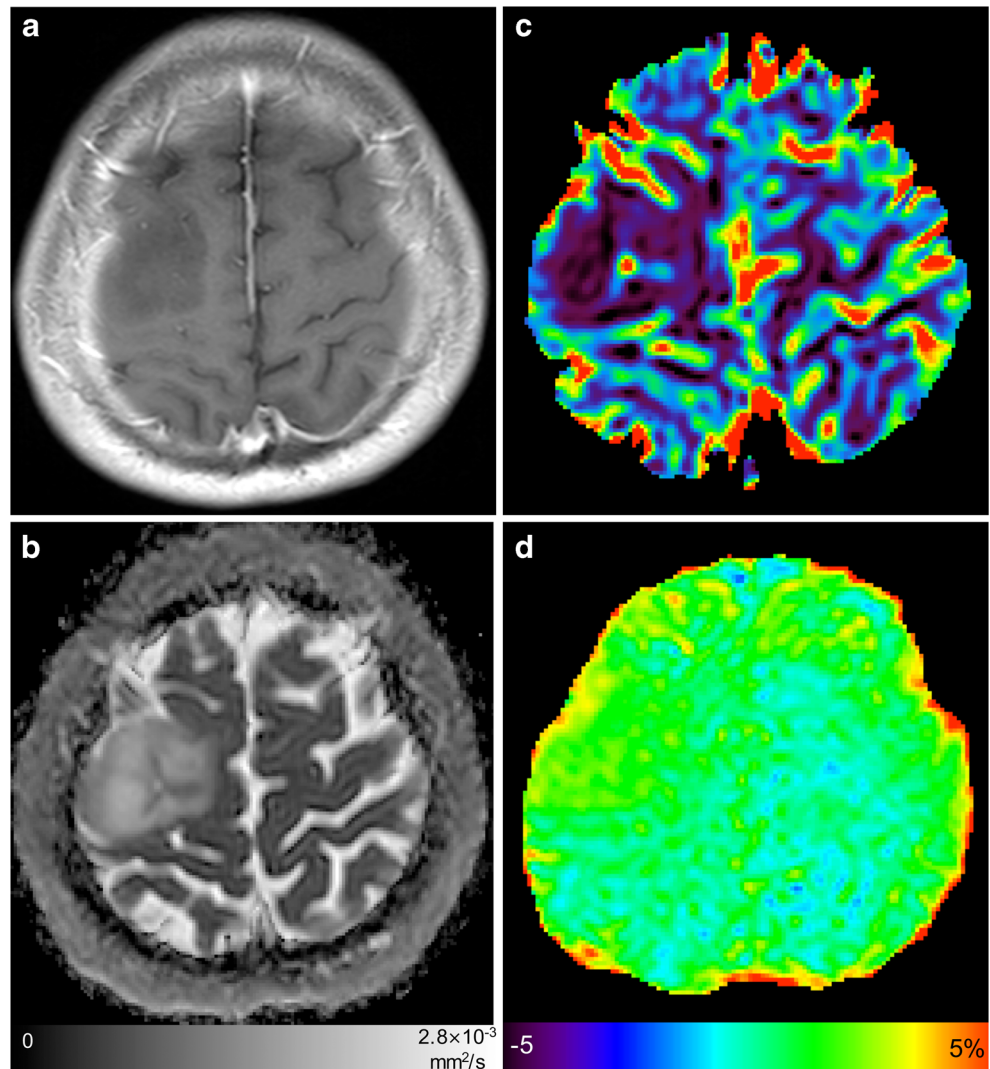
Inter-observer agreement

The mean size of segmented regions by observer 1 (1212 ± 779 mm²) was significantly smaller than that by observer 2 (1456 ± 886 mm²). Table 2 shows the ICCs of the measurements by the two observers. Excellent agreement was observed for APT₉₀, rCBV₉₀, APT_{mean}, ADC_{mean}, and rCBV_{mean}, but not for ADC₁₀.

Comparisons of the parameters between LGGs and HGGs

Table 3 shows the parameter measurements in the LGG and HGG groups. The APT₉₀ (*P* = 0.001) and APT_{mean} (*P* = 0.0001) were significantly larger in the HGG group compared to the LGG group. The ADC₁₀, ADC_{mean}, rCBV₉₀, and rCBV_{mean} values were not significantly different between the

Fig. 4 A 38-year-old male with a diffuse astrocytoma. (a) The post-contrast T1-weighted image showed no contrast enhancement (CE) in the tumour in the right frontal lobe. (b) The ADC map revealed a high ADC value ($ADC_{10} = 0.99 \times 10^{-3} \text{ mm}^2/\text{s}$) of the tumour compared to the normal white matter. (c) The rCBV map showed low rCBV ($rCBV_{90} = 2.78$) in the tumour. (d) The APT-weighted image showed only a mild increase in APT signal ($APT_{90} = 2.15 \%$) in the tumour



two groups. The diameter of HGG ($56.4 \pm 20.1 \text{ mm}$) was significantly larger than that of LGG ($43.8 \pm 14.1 \text{ mm}$).

Correlation among the parameters

The APT_{90} significantly correlated with the $rCBV_{90}$ ($r = 0.42$, $P = 0.01$). The other comparisons among the APT signal, ADC and rCBV did not show significant correlations. The diameter of the tumour did not correlate with the APT signal, ADC, and rCBV.

Diagnostic performance in differentiating HGGs from LGGs

Table 4 and Fig. 3 summarize the diagnostic performance of the parameters as determined by the ROC analyses. Medium diagnostic performance was achieved by the APT_{90} , with the AUC of 0.811, and by the APT_{mean} with the AUC of 0.886. APT_{90} showed 85.7 % sensitivity and 70.0 % specificity with the cutoff value of 2.92 %. APT_{mean} showed 71.4 % sensitivity and 95.0 %

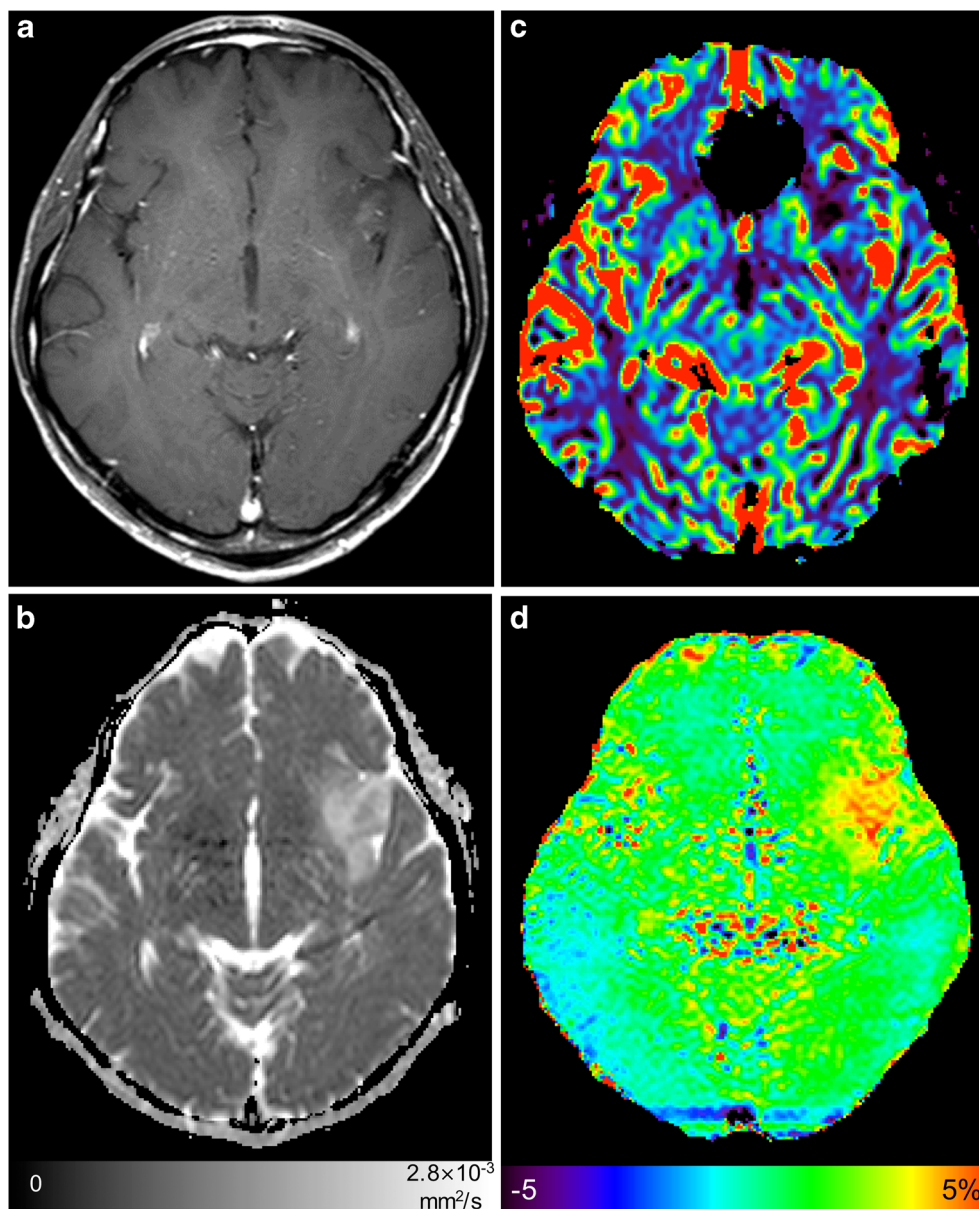
specificity with the cutoff value of 2.56 %. The ADC_{10} , ADC_{mean} , $rCBV_{90}$, and $rCBV_{\text{mean}}$ resulted in low diagnostic performance. The comparisons of ROC curves revealed that the AUC of APT_{90} was significantly higher than those of ADC_{10} and $rCBV_{90}$ ($P < 0.05$), and the AUC of APT_{mean} was significantly higher than those of ADC_{mean} and $rCBV_{\text{mean}}$ ($P < 0.05$).

Figures 4 and 5 show representative cases of grade II (diffuse astrocytoma) and grade III (anaplastic oligodendroglioma), respectively. Although little CE was seen in both cases, the grade III glioma had a higher APT signal than the grade II glioma. Note that a high APT signal was extensively observed within the tumour, which resulted in a higher APT_{mean} value.

Discussion

The results of the present study demonstrated the diagnostic performance of APT imaging for grading diffuse gliomas with

Fig. 5 A 47-year-old male with an anaplastic oligodendroglioma. (a) A post-contrast T1-weighted image showed only slight CE in the tumour in the left insula. (b) The ADC map revealed a high ADC value ($ADC_{10} = 1.48 \times 10^{-3} \text{ mm}^2/\text{s}$) of the tumour compared to the normal white matter. (c) The rCBV map showed reduced rCBV ($rCBV_{90} = 2.34$) in the tumour. (d) The APT-weighted image revealed an increase in the APT signal ($APT_{90} = 4.19 \%$) in the tumour



no or little CE. We found a significant increase in the APT_{90} and APT_{mean} values in the HGGs compared to the LGGs.

The sources of the APT signal and contrast are a matter of controversy. The high APT signal in tumours can be attributed to abundant concentration of mobile proteins and peptides in cellular cytoplasm. Higher cell density reported in HGGs in a human study [22] and animal study [23] would be a cause of higher concentration of mobile proteins and peptides. The present results revealed that the ADC did not differ between the high and low grades, indicating that the cell density was not very different between the grades whereas the APT signals were clearly different between the grades. This is consistent with the previous study which demonstrated that APT signal shows a weak correlation with cell density in diffuse gliomas [13]. These results suggested that the concentrations of mobile

proteins and peptides included in the intracellular space are increased in HGGs compared to LGGs. The proteins and peptides in the extracellular space (such as interstitial fluid, mucin, or microcysts) could contribute to the increase in the APT signal in gliomas, if they are different between the grades. The APT signal could be also affected by changes in the nuclear Overhauser effect (NOE) in tissue [24, 25]. Thus, overall, further investigations are needed to determine the mechanisms of the APT contrast in tumours.

Regarding the differentiation of low and high grades in nonenhancing gliomas, Lee et al. reported that the minimum ADC was useful although substantial overlaps were observed between LGGs and HGGs [8]. In our present study, however, ADC_{10} failed in this discrimination. The inter-observer agreement for ADC_{10} was not high, despite the excellent agreement

for ADC_{mean} . This result indicated that ADC_{10} originated from the tumour boundary area, rather than the tumour core, in which the location of the regions-of-interest could differ between the two observers. The boundary area consists of the mixture of infiltrating glioma cells and normal brain tissue. Since normal white matter has lower ADCs than most types of tumorous tissue, ADC_{10} might reflect the content of normal brain tissue rather than the cell density of gliomas. This could be a limitation of the histogram analysis of the ADC in evaluating infiltrating gliomas.

Falk et al. reported using DSC PW imaging; they observed that $rCBV_{90}$ was significantly higher in grade III compared to grade II nonenhancing gliomas ($P=0.04$) [9]. Although two of our present HGG cases had $rCBV$ values >10.00 and although the $rCBV$ tended to be higher in our HGG group, no significant difference was found between the two groups. These parameters could still be valuable to investigate in a larger cohort.

We found that the APT_{90} significantly correlated with the $rCBV_{90}$. This correlation might indicate that the increase in cytoplasmic proteins and peptides in glioma cells is associated with neoangiogenesis.

In the CEST imaging, long saturation pulses are necessary to accumulate saturated protons in bulk water; however, the length of the saturation pulse was limited to <1 s in previous studies, due to typical limitations of the RF amplifiers in clinical MRI systems. This problem was solved in the present study by using the two amplifiers of a parallel transmission system in alternation [15, 16], enabling 2 s of saturation at 100 % duty-cycle. A 2012 study showed that the APT contrast obtained with the 2-s saturation was higher than the corresponding values obtained with 0.5-s or 1-s saturation in various types of human brain tumours including gliomas [26]. Since CEST imaging is highly sensitive to B_0 inhomogeneity, shimming and correction for B_0 inhomogeneity in the post-processing are crucial. The accuracy and reproducibility of the APT imaging scheme used in the present study was confirmed in patients with various types of brain tumour [16].

The present study has several limitations. First, the cohort is relatively small, especially that of the HGGs ($n=14$) which usually show CE. The sample size was not large enough to perform separate analyses of astrocytomas and oligodendrogliomas. Second, single slice acquisition was employed in the APT imaging sequence due to the limitation of the total acquisition time in the clinical patient scans. Thus, it was not possible to cover the entire tumour. However, a recent study showed that diagnostic performance of a single slice APT imaging was equivalent to that of multi-slice imaging in grading gliomas [14]. Protocols with fast three-dimensional (3-D) coverage are now under development to better characterize the typical tumour tissue heterogeneity in all

dimensions. Finally, the histopathological diagnoses were based on a biopsy in three patients with HGG, and all of the other patients' diagnoses were based on resected specimens. The amount or fraction of high grade component within a tumour might have influenced the results in the biopsy cases. However, we expect that the histogram approach should have been still effective in those cases.

In conclusion, the APT_{90} and APT_{mean} were significantly higher in the HGGs than in the LGGs, whereas no significant differences were found in ADCs and $rCBV$ values in these gliomas without intense CE. The APT_{90} and APT_{mean} showed medium diagnostic performance in the discrimination of the HGG and LGG groups. APT imaging, which produces an endogenous contrast based on saturation transfer, may be useful in the prediction of the histopathological malignancy of diffuse gliomas without CE.

Acknowledgments The scientific guarantor of this publication is Hiroshi Honda.

The authors of this manuscript declare relationships with the following companies: Jochen Keupp is an employee of Philips Research Europe, and Masami Yoneyama is an employee of Philips Electronics Japan. This study has received funding by the Japanese Society of Neuroradiology, Japanese Radiological Society, the Fukuoka Foundation for Sound Health Cancer Research Fund, and JSPS KAKENHI Grants-in-Aid for Scientific Research nos. 26461827, 26293278, 26670564 and 22591340. No complex statistical methods were necessary for this paper. Institutional Review Board approval was obtained. Written informed consent was waived by the Institutional Review Board.

Methodology: retrospective, diagnostic or prognostic study, performed at one institution.

References

1. Daumas-Duport C, Scheithauer B, O'Fallon J, Kelly P (1988) Grading of astrocytomas. A simple and reproducible method. *Cancer* 62:2152–2165
2. Law M, Yang S, Babb JS et al (2004) Comparison of cerebral blood volume and vascular permeability from dynamic susceptibility contrast-enhanced perfusion MR imaging with glioma grade. *AJNR Am J Neuroradiol* 25:746–755
3. Hilario A, Sepulveda JM, Perez-Nunez A et al (2014) A prognostic model based on preoperative MRI predicts overall survival in patients with diffuse gliomas. *AJNR Am J Neuroradiol* 35:1096–1102
4. Pierallini A, Bonamini M, Bozzao A et al (1997) Supratentorial diffuse astrocytic tumours: proposal of an MRI classification. *Eur Radiol* 7:395–399
5. Mihara F, Numaguchi Y, Rothman M, Sato S, Fiandaca MS (1995) MR imaging of adult supratentorial astrocytomas: an attempt of semi-automatic grading. *Radiat Med* 13:5–9
6. Fan GG, Deng QL, Wu ZH, Guo QY (2006) Usefulness of diffusion/perfusion-weighted MRI in patients with non-enhancing supratentorial brain gliomas: a valuable tool to predict tumour grading? *Br J Radiol* 79:652–658
7. McKnight TR, Lamborn KR, Love TD et al (2007) Correlation of magnetic resonance spectroscopic and growth characteristics within Grades II and III gliomas. *J Neurosurg* 106:660–666

8. Lee EJ, Lee SK, Agid R, Bae JM, Keller A, Terbrugge K (2008) Preoperative grading of presumptive low-grade astrocytomas on MR imaging: diagnostic value of minimum apparent diffusion coefficient. *AJNR Am J Neuroradiol* 29:1872–1877
9. Falk A, Fahlstrom M, Rostrup E et al (2014) Discrimination between glioma grades II and III in suspected low-grade gliomas using dynamic contrast-enhanced and dynamic susceptibility contrast perfusion MR imaging: a histogram analysis approach. *Neuroradiology* 56:1031–1038
10. Zhou J, Payen JF, Wilson DA, Traystman RJ, van Zijl PC (2003) Using the amide proton signals of intracellular proteins and peptides to detect pH effects in MRI. *Nat Med* 9:1085–1090
11. Zhou J, Lal B, Wilson DA, Laterra J, van Zijl PC (2003) Amide proton transfer (APT) contrast for imaging of brain tumors. *Magn Reson Med* 50:1120–1126
12. Zhou J, Blakeley JO, Hua J et al (2008) Practical data acquisition method for human brain tumor amide proton transfer (APT) imaging. *Magn Reson Med* 60:842–849
13. Togao O, Yoshiura T, Keupp J et al (2014) Amide proton transfer imaging of adult diffuse gliomas: correlation with histopathological grades. *Neuro Oncol* 16:441–448
14. Sakata A, Okada T, Yamamoto A et al (2015) Grading glial tumors with amide proton transfer MR imaging: different analytical approaches. *J Neurooncol* 122:339–348
15. Keupp J, Baltes C, Harvey P, Van den Brink J (2011) Parallel RF transmission based MRI technique for highly sensitive detection of amide proton transfer in the human brain at 3T. *Proc Int Soc Magn Reson Med* 19:710
16. Togao O, Hiwatashi A, Keupp J et al (2015) Scan-rescan reproducibility of parallel transmission based amide proton transfer imaging of brain tumors. *J Magn Reson Imaging* 42:1346–1353
17. Boxerman JL, Schmainda KM, Weisskoff RM (2006) Relative cerebral blood volume maps corrected for contrast agent extravasation significantly correlate with glioma tumor grade, whereas uncorrected maps do not. *AJNR Am J Neuroradiol* 27:859–867
18. Hu LS, Eschbacher JM, Heiserman JE et al (2012) Reevaluating the imaging definition of tumor progression: perfusion MRI quantifies recurrent glioblastoma tumor fraction, pseudoprogression, and radiation necrosis to predict survival. *Neuro Oncol* 14:919–930
19. Paulson ES, Schmainda KM (2008) Comparison of dynamic susceptibility-weighted contrast-enhanced MR methods: recommendations for measuring relative cerebral blood volume in brain tumors. *Radiology* 249:601–613
20. Thevenaz P, Ruttimann UE, Unser M (1998) A pyramid approach to subpixel registration based on intensity. *IEEE Trans Image Process* 7:27–41
21. Shrout PE, Fleiss JL (1979) Intraclass correlations: uses in assessing rater reliability. *Psychol Bull* 86:420–428
22. Wen Z, Hu S, Huang F et al (2010) MR imaging of high-grade brain tumors using endogenous protein and peptide-based contrast. *Neuroimage* 51:616–622
23. Salhotra A, Lal B, Laterra J, Sun PZ, van Zijl PC, Zhou J (2008) Amide proton transfer imaging of 9L gliosarcoma and human glioblastoma xenografts. *NMR Biomed* 21:489–497
24. Xu J, Zaiss M, Zu Z et al (2014) On the origins of chemical exchange saturation transfer (CEST) contrast in tumors at 9.4 T. *NMR Biomed* 27:406–416
25. Heo HY, Zhang Y, Lee DH, Hong X, Zhou J (2015) Quantitative assessment of amide proton transfer (APT) and nuclear overhauser enhancement (NOE) imaging with extrapolated semi-solid magnetization transfer reference (EMR) signals: application to a rat glioma model at 4.7 tesla. *Magn Reson Med*. doi:10.1002/mrm.25581
26. Togao O, Yoshiura T, Keupp J et al (2012) Effect of saturation pulse length on parallel transmission based Amide Proton Transfer (APT) imaging of different brain tumor types. *Proc Int Soc Magn Reson Med* 21:744